Microscale Glass-Blown Three-Dimensional Spherical Shell Resonators

Igor P. Prikhodko, *Student Member, IEEE*, *Member, ASME*, Sergei A. Zotov, *Member, IEEE*, Alexander A. Trusov, *Member, IEEE*, *Member, ASME*, and Andrei M. Shkel, *Senior Member, IEEE*

***Abstract*—This paper introduces a new paradigm for design and batch fabrication of isotropic 3-D spherical shell resonators. The approach uses pressure and surface tension driven plastic deformation (glassblowing) on a wafer scale as a mechanism for creating inherently smooth and symmetric 3-D resonant structures. The feasibility of the new approach was demonstrated by fabrication and characterization of Pyrex glass spherical shell resonators with millimeter-scale diameter and average thickness of 10 μm. Metal electrodes cofabricated along with the shell were used to actuate the two dynamically balanced four- and six-node vibratory modes. For 1-MHz glass-blown resonators, the relative frequency mismatch $\Delta f / f$ between the two degenerate four-node wineglass modes was measured as 0.63% without any trimming or tuning. For the higher order six-node wineglass modes, the relative frequency mismatch was only 0.2%, demonstrating the potential for precision manufacturing. The intrinsic manufacturing symmetry enabled by the technology may inspire new classes of high-performance 3-D MEMS for communication and inertial navigation. [2010-0268]**

***Index Terms*—Fabrication, glass, glassblowing, microscale sphere, resonator, spherical shell, vibration, wafer-level micromachining, wineglass mode, 3-D MEMS.**

I. Introduction

MINIATURE resonators are required for a number of applications, including signal processing, timing, frequency control, and inertial sensing [1]. A wide variety of surface and bulk fabrication technologies for silicon MEMS resonators has been developed over the past decades, with several commercial silicon resonators currently entering the consumer electronics markets [2]–[4]. A majority of technologies for MEMS resonator fabrication rely on photolithography and silicon DRIE, with reported relative fabrication tolerances on the order of 1% [5]. The well-known limitations of these technologies are the fabrication imperfections introduced by etching, such as DRIE-induced scalloping, surface roughness, footing effects, and aspect ratio constraints. As a result, the fabrication of highly symmetric devices, frequency matching, maximization of quality factor, and further device miniaturization without performance sacrifice become challenging. These factors motivate the investigation of alternative nonplanar architectures and technologies for resonant MEMS with increased symmetry, reduced roughness, and increased aspect ratios—all accomplished simultaneously.

Among the shell-type vibrating elements [6], spherical shells are promising candidates for resonant 3-D MEMS architectures due to their structural symmetry, rigidity, and low energy losses through the shell support. Large surface area and sphericity also account for uniform thermal distribution and reduced thermal gradients. In addition, operation of dynamically balanced wineglass modes in 3-D axisymmetric shells provides increased robustness to fabrication imperfections. This is due to the fact that the natural frequencies of clamped spherical shells have weak dependence on thickness variations [7] as compared to mass-spring type resonators. These considerations motivate the development of batch micromachined spherical shell resonators.

Until recently, micromachining of shell-type structures was limited to isotropic etch of silicon spherical bowls [8], [9] and LIGA process for cylindrical shells [10]. These technologies are based on lithography and selective etching, leading to detrimental fabrication imperfections such as surface roughness and scalloping. Fabrication of solid microspheres was developed for nanophotonics applications, including high-temperature fusion of quartz fibers [11] and resistive heating of chalcogenide glass [12]. Manufacturing of spherical shells was demonstrated on a centimeter scale for bulk metallic glasses [13]. We report an alternative wafer-level approach for the batch micromachining of axisymmetric 3-D resonant shells.

This paper explores the hypothesis that plastic deformation driven by surface tension and differential gas pressure, or glassblowing [14], may serve as an enabling mechanism for wafer-scale fabrication of highly smooth and symmetric 3-D spherical shell resonators. The technique of Pyrex glassblowing was previously introduced for the creation of spherical cells for chip-scale atomic devices [15], [16]. The micromachining approach proposed in this paper allows simultaneous fabrication of spherical shells along with actuation and detection electrodes. The process consists of the following: 1) bonding a Pyrex glass wafer on a silicon substrate with pre-etched cavities; 2) patterning flat metal features on the silicon-on-glass substrate; and 3) heating the wafer stack above the softening point of glass. The temperature-induced plastic deformation

Manuscript received September 11, 2010; revised December 19, 2010; accepted February 8, 2011. Date of publication April 15, 2011; date of current version June 2, 2011. This work was supported in part by the NSF under Grant CMMI-0928999 (Program Manager Shih-Chi Liu) and in part by DARPA/SPAWAR under Grant N66001-10-1-4074 (Program Manager Tayo Akinwande). I. P. Prikhodko and S. A. Zotov contributed equally to this work. Subject Editor Y. B. Gianchandani.

The authors are with the Department of Mechanical and Aerospace Engineering, MicroSystems Laboratory, University of California, Irvine, CA 92697 USA (e-mail: iprikhod@uci.edu; szotov@uci.edu; atrusov@uci.edu; ashkel@uci.edu).

Color versions of one or more of the figures in this paper are available online at http://ieeexplore.ieee.org.

Digital Object Identifier 10.1109/JMEMS.2011.2127453

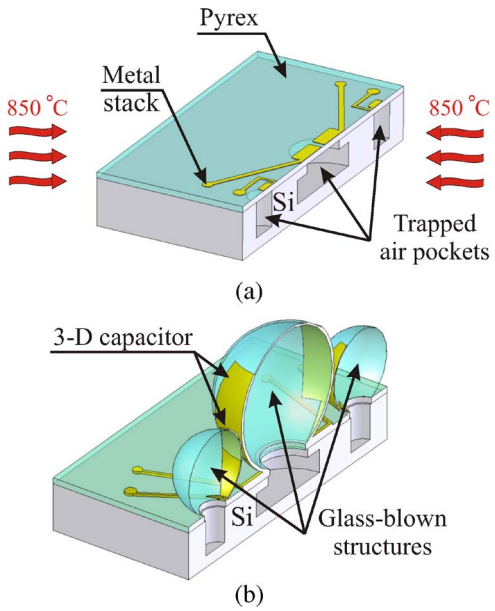

Fig. 1. Conceptual schematics of a 3-D spherical shell resonator fabrication using wafer-scale metal-on-glass stack glassblowing. (a) Planar structure before glassblowing. (b) Three-dimensional structure after glassblowing.

of the metal-on-glass stack creates 3-D spherical shells with integrated metal electrodes (Fig. 1).

This paper is organized into four sections. Section II analyzes the natural frequencies and mode shapes of a spherical shell, including the effects of fabrication imperfections on the resonant frequency. Experimental characterization of resonant modes, demonstrating the potential of glass-blown shells as high-quality mechanical vibratory elements using off-chip excitation, is presented in Section III. Section IV describes the novel fabrication process for the integration of on-chip 3-D metal electrodes, including electromagnetic and electrostatic transducer architectures. Finally, Section V experimentally verifies the feasibility of 3-D resonant shell resonators with integrated transduction.

II. Free Vibration of Spherical Shells

This section analyzes the natural frequencies and mode shapes of glass-blown microshells. The modeling assumes that spherical shells are thin, elastic, and rigidly clamped at the edge and that they satisfy Kirchhoff–Love assumptions [17]. The assumptions are valid for the nominal geometry, shown in Fig. 2.

A. Spherical Shell Natural Frequencies

The general differential equations of spherical shell motion were derived by van der Neut [18] and Havers [19] for the static case and later by Federhofer [20] and Novozhilov [21], [22] for the dynamic case (see the Appendix). The closed-form analytical solution of these equations is limited to the static case [21] since the vibration spectrum analysis of spherical shells with arbitrary boundaries is intricate [23]. The expression for natural frequencies f_m in the closed form was derived in [7].

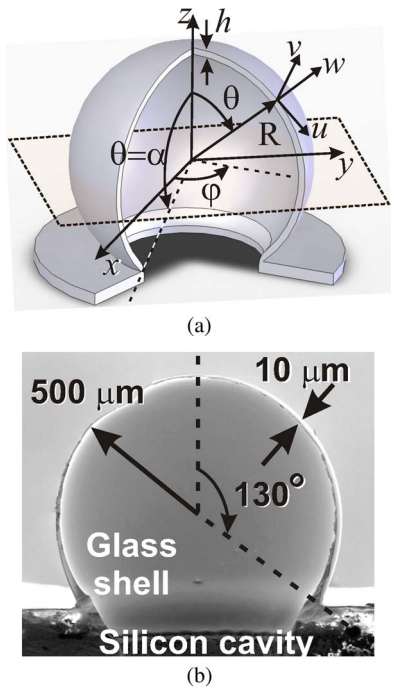

Fig. 2. Parameters for the analysis of a glass-blown spherical shell. (a) Notations and geometry of a spherical shell clamped at the edge. (b) SEM cross-sectional image of a fabricated shell with nominal geometry.

For a spherical shell (Fig. 2) with shell radius R, thickness h, edge angle α, Young's modulus E, Poisson's ratio ν, and volumetric mass density ρ

$$f_m = \frac{1}{2\pi}\frac{k_m}{R}\sqrt{\frac{E}{\rho(1-\nu^2)}}. \tag{1}$$

Here, k_m is a dimensionless frequency parameter for the natural frequency of a vibratory mode of order m and is calculated for each m given a set of boundary conditions. As shown in the Appendix, for a clamped spherical shell with $p_i = p_i(\alpha)$ defined by the boundary conditions at the edge angle $\theta = \alpha$, frequency parameter k_m for each p_i satisfies

$$k_m^4 - \left[p_i + 1 + 3\nu + (1-\nu^2)\frac{p_i^2}{c^2}\right]k_m^2 + (1-\nu^2)\left[p_i - 2 + p_i^2\frac{p_i - 4}{c^2}\right] = 0 \tag{2}$$

where $c^2 = 12(1-\nu^2)R^2/h^2$.

The analysis of the coefficients of biquadratic eq. (2) shows that the frequency parameter k_m depends on three physical parameters: Poisson's ratio ν, radius-to-thickness ratio R/h, and edge angle $\alpha[k_m = k_m(\nu, R/h, \alpha)]$. The dimensionless values k_m were calculated using (2) for the typical geometry of a micromachined Pyrex shell [Fig. 2(b)], assuming that $R = 0.5$ mm, $h = 10$ μm, $\alpha = 130°$, $\nu = 0.2$, $E = 64$ GPa, and $\rho = 2.23$ g/cm^3, and were converted to the frequency values f_m using (1). The natural frequencies summarized in Table I for each vibratory mode $m = 0, 1, 2, 3$ revealed the spectrum of vibrations in a megahertz range.

TABLE I
NATURAL FREQUENCIES OF PYREX 7740 SPHERICAL SHELL WITH NOMINAL GEOMETRY FROM FIG. 2 (IN KILOHERTZ)

Mode m	Bouncing 0	Rocking 1	Wineglass 2	Wineglass 3
Theory				
Equations (1)-(2), f_m	1403	811	1352	1522
k_m (dimensionless)	0.806	0.466	0.777	0.874
FEM, 80420 nodes	1357	799	1291.4	1556.52
FEM, 32310 nodes	1360	825	1291.45	1556.53
FEM, 14340 nodes	1365	868	1291.55	1556.57
Experiment				
Sample no. 1	1193	677, 687	1270, 1279	1433, 1436
Measured $\Delta f/f$	NA	1.4 %	0.71 %	0.21 %
Sample no. 2	1186	689, 698	1266, 1274	1444, 1447
Measured $\Delta f/f$	NA	1.3 %	0.63 %	0.21 %

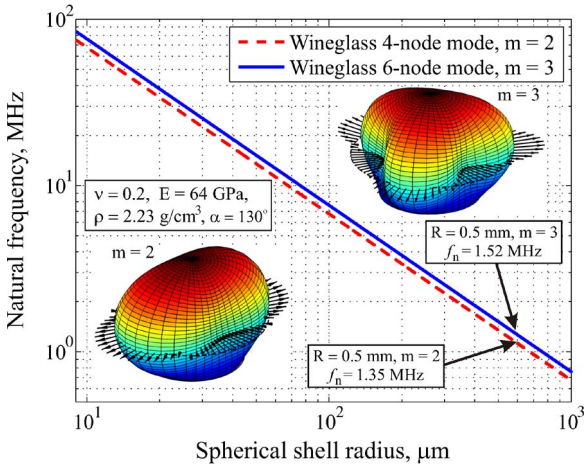

Fig. 3. Scaling of the wineglass vibratory modes $m = 2, 3$ as a function of the spherical shell size, calculated for Pyrex glass (material parameters are included). (Insets) Spherical shell shape mode shapes and velocity distribution at the equator.

The natural frequencies can be scaled by design using (1) and (2) to meet application-specific requirements. Fig. 3 shows the effects of shell radius on the natural frequencies of wineglass modes $m = 2, 3$, calculated using (1). Since the natural frequency f_m is inversely proportional to the shell radius R, higher frequencies can be obtained by reducing the radius (assuming constant R/h). The theoretical analysis is compared with finite element (FE) modeling in the next section.

B. Spherical Shell Mode Shapes

FE modal analysis was performed using MSC Patran to analyze the mode shapes of glass-blown shells and to compare with frequency values predicted theoretically. The modes shown in Fig. 4 are classified by the order m, which corresponds to half of the number of nodal lines (points of zero displacement) of the spherical shell. The resonant frequencies of modes $m = 0, 1, 2, 3$ are summarized for different mesh densities in Table I.

The first bouncing mode [$m = 0$; Fig. 4(a)] corresponds to the extension–compression of the sphere along the axis of symmetry. This motion results in a uniform radial distribution of displacement vectors, illustrated for the horizontal cross section. The rocking mode [$m = 1$; Fig. 4(b)] involves side bending of the shell, which is seen in a horizontal cross section as an in-plane translation of every surface point except for the two nodes. The mode $m = 1$ is degenerate, and its second counterpart is spatially oriented 90° relative to the first.

When the shell vibrates in symmetric and dynamically balanced wineglass mode ($m = 2$), there are four equally spaced polar zones [Fig. 4(c)]. Neighboring zones move in opposite directions with an 180° alternating phase. The degenerate counterparts of the four-node wineglass modes are spatially oriented 45° relative to each other. For the higher order wineglass mode $m = 3$, there are six nodal lines dividing the resonant shell in polar zones [Fig. 4(d)]. This mode is also degenerate, and its counterparts are spatially oriented 30° relative to each other.

The four- and six-node modes are dynamically balanced and provide inherent rejection of common mode accelerations. These modes are preferred for operation in harsh environments [1]. The resonant frequencies obtained by FE modeling for the same parameters ($R = 0.5$ mm, $h = 10$ μm, $\alpha = 130°$, $\nu = 0.2$, $E = 64$ GPa, and $\rho = 2.23$ g/cm^3) are within 3% of the frequency values predicted by (1) and (2), validating the modeling approach (see Table I).

C. Effect of Boundary Variations on Frequency

Glass-blown shells operating in wineglass resonant modes are inherently robust against variations of boundary conditions at the edge. Fig. 5 shows the effect of boundary variations on natural frequencies calculated by varying parameter $p_i(\alpha)$ of (2). The boundary of the edge $\theta = \alpha$ formed during glassblowing depends on the geometry of a sealed silicon cavity, which affects the natural frequency. The frequencies of shell structures with $\alpha < 130°$ [including circular membranes ($\alpha < 40°$) and hemispherical shells ($\alpha = 90°$)] show a notable change with edge angle variation. In contrast, frequencies of spherical shells ($\alpha > 130°$) are minimally affected in a flat region $130° < \alpha < 180°$ (Fig. 5) and have no significant deviation from the complete shell frequencies. This observation led to the insight that glass-blown spherical shells (typically $\alpha \geq 130°$) operating in wineglass modes are more resistant to boundary variations, hence less susceptible to fabrication imperfections.

D. Effect of Thickness Variations on Frequency

Rigidly clamped spherical shells provide increased resistance to such fabrication imperfections as a thickness variation. The frequency sensitivity to the thickness change was evaluated for rigidly clamped (fixed edge) and wineglass (free edge) spherical shells and was compared to mass-spring type resonators. Normalized natural frequencies of a spherical shell with $\alpha = 130°$ were calculated from biquadratic eq. (2) by varying thickness h and were shown in Fig. 6. As expected, the clamped spherical shells exhibit weak dependence on the thickness (for modes $m = 2, 3$). This fact was also supported by theoretical analysis of thin elastic shells [7]. In contrast, the natural frequency of wineglass structures scales linearly with h according to Loper *et al.* [24]. The same analysis for conventional planar mass-spring type resonators shows a strong sensitivity of frequency f to variation w in the beam width $f \propto w^{3/2}$ [25]. As shown in Fig. 6, the frequency dependence

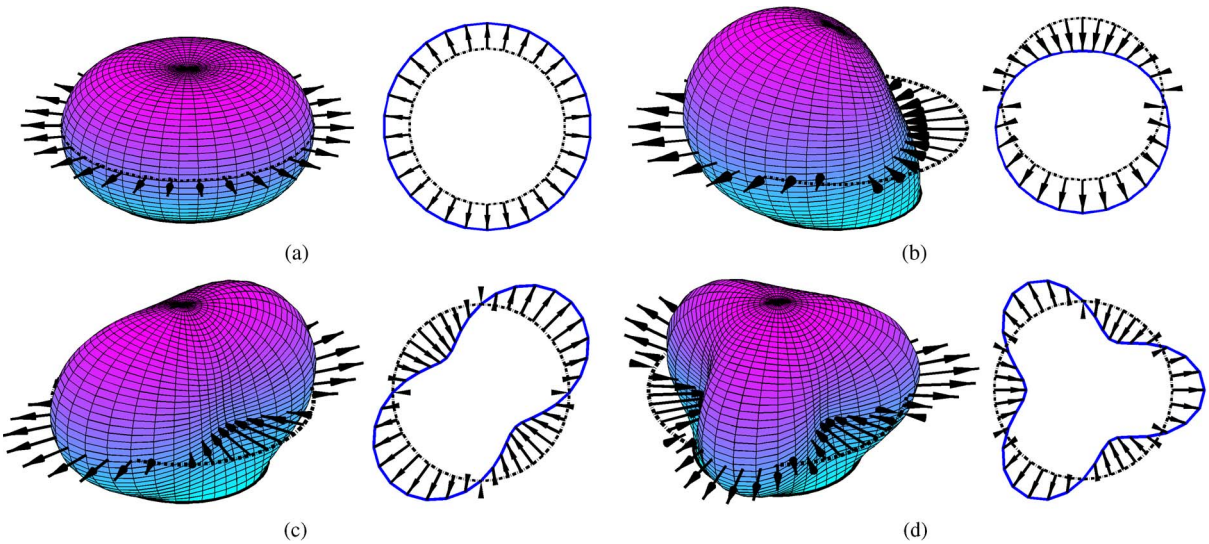

Fig. 4. Vibratory mode shapes of a clamped spherical shell, showing displacement distribution in 3-D and horizontal cross section. (a) Bouncing mode ($m = 0$). (b) Rocking mode ($m = 1$). (c) Wineglass four-node mode ($m = 2$). (d) Wineglass six-node mode ($m = 3$).

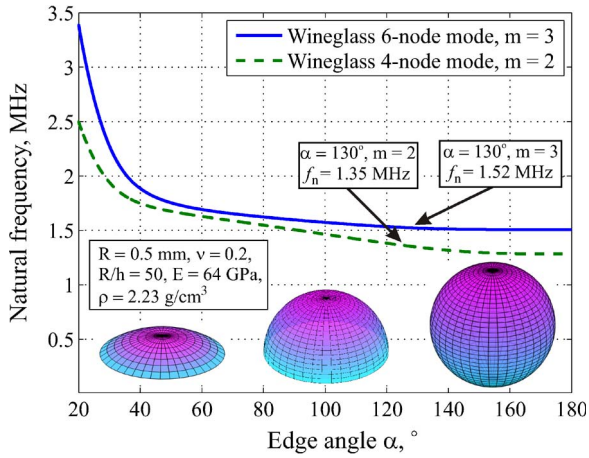

Fig. 5. Dependence of the natural frequencies on the edge angle α for modes $m = 2, 3$, calculated for Pyrex spherical shell. The physical parameters are included.

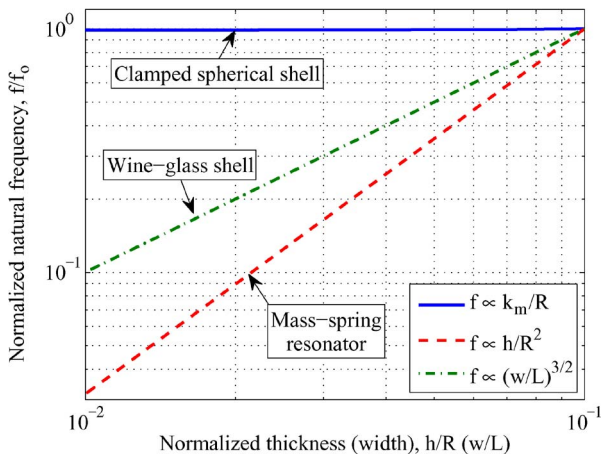

Fig. 6. Dependence of the natural frequencies on the thickness h for spherical shells and width w for mass-spring type resonators. Shell radius R and beam length L are fixed. Rigidly clamped shells demonstrate weak dependence on thickness.

on thickness variation for a clamped spherical shell with $h/R = 0.02$ is one order of magnitude lower than that for similar mass-spring type resonators. This consideration motivates the development of micromachined spherical shell resonators.

III. Glass-Blown Shell as a Vibratory Element

This section reports fabrication and experimental characterization of mode shapes and structural isotropy of fabricated prototypes using an off-chip transducer. Multiple wafer-level runs were performed to optimize the processing parameters. The experimental data presented here rely on two fully characterized samples, which were fabricated in the same batch.

A. Spherical Shell Fabrication

The fabrication of 3-D resonant shells presented in this paper relies on wafer-scale glassblowing, which was previously developed for the creation of symmetric spherical cells for chip-scale atomic devices [16]. The process starts by hermitically bonding a 100-μm-thick Corning Pyrex 7740 glass wafer to a silicon wafer with an array of 0.5-mm-diameter cylindrical cavities etched 0.8 mm deep [Fig. 1(a)]. The wafer stack is then heated above the 850-°C softening point of Pyrex glass. Above this temperature, the viscosity of glass reduces, and the expansion of the air trapped inside the pre-etched silicon cavities causes the flat glass to be blown into symmetric spherical shapes [Fig. 1(b)]. The formation of 1-mm-diameter shells is deemed independent from the glass weight. As shown in [26], the effect of gravity g is negligible for shell sizes r less than the capillary length value $[r < k^{-1} = \sqrt{\gamma/(\rho g)}]$, which is approximately 3.4 mm for molten borosilicate glasses with a surface tension of $\gamma = 260 \cdot 10^{-3}$ N/m [27] and a density of $\rho = 2230$ kg/m^3.

B. Surface Metrology

Surface roughness is a known performance limiting factor in microscale resonators [28]. The pressure and surface tension

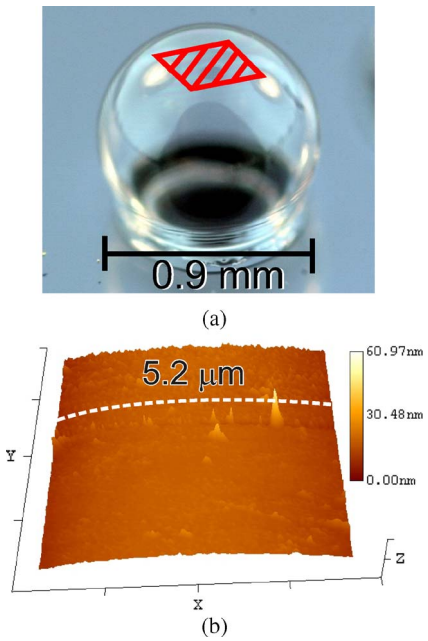

Fig. 7. Surface roughness of a glass shell measured with an AFM. The relative roughness is 1 ppm (roughness/diameter). (a) 1-mm glass-blown shell with marked 5.2×5.2 μm^2 area of measurement. (b) Surface measurement indicates 0.85-nm average surface roughness. The color legend is the curvature radius of the scanned area.

driven glassblowing process is expected to provide surface roughness improvement compared to the conventional fabrication processes based on etching. To investigate this hypothesis experimentally, several glass-blown shells were characterized using an Agilent Nano R2 atomic force microscope (AFM). The initial average surface roughness of the Pyrex 7740 substrate before glassblowing was measured as 0.48 nm over a 5.2×5.2 μm^2 area. The average surface roughness after the fabrication was measured as 0.85 nm on the outer shell surface. This translates into a surface-roughness-to-size ratio of 1 ppm relative to the 1 mm diameter of the shell (Fig. 7). The uncertainty of both AFM measurements was on the order of ± 0.2 nm. The final shell roughness is comparable to the initial glass roughness before the fabrication. Further reduction in shell roughness can be achieved by controlling the level of glass impurities and contaminants in the nitrogen atmosphere of the glassblowing furnace.

To compare the glassblowing technology with conventional micromachining, the same set of measurements was performed on a sidewall of a silicon resonator defined by DRIE using Unaxis Versaline VL-7339. The surface defects were measured as 17 nm over the same area, which is equivalent to a surface-roughness-to-size ratio of 167 ppm relative to the 100-μm beam thickness. This comparison demonstrates the potential of the glassblowing technology to produce 3-D resonators with very low surface roughness.

C. Experimental Identification of Mode Shapes

Inherent fabrication symmetry and measured low surface roughness suggest that glass-blown spheres can serve as high-quality resonant structures with superior degree of isotropy.

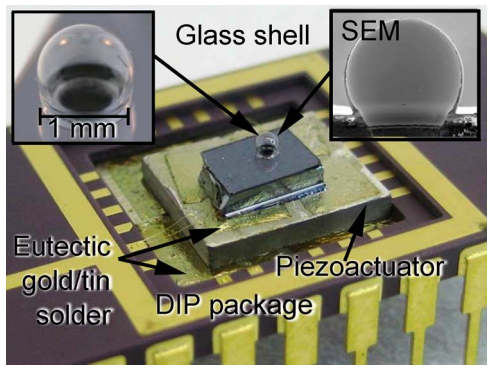

Fig. 8. Photograph of a packaged glass-blown shell bonded to a piezoelectric actuator for structural mode characterization.

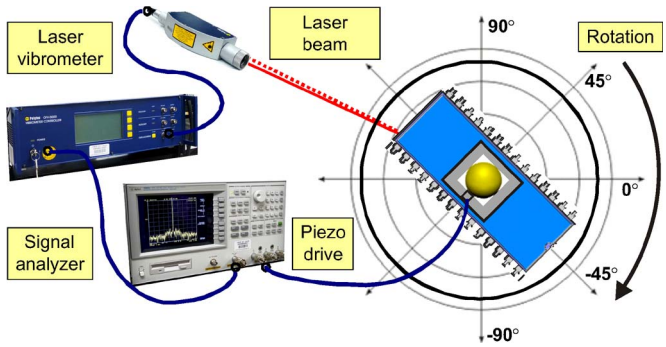

Fig. 9. Schematics of the experimental testbed for noncontact characterization of glass-blown shells using a laser vibrometer.

This section investigates the resonant properties of fabricated spheres using noncontact characterization methods facilitated by a Laser Doppler Vibrometer (LDV). For the experiment, a 3-D shell die was eutectically bonded to a piezoelectric plate actuator and was packaged in a ceramic 24-pin DIP (Fig. 8). The piezoelectric layer was chosen in the preliminary experiments for the excitation of multiple-order vibratory modes on a spatial 3-D structure. A Polytec OVF-5000 single-point LDV was used to directly measure velocities of surface points on the vibrating shell in real time.

For the experimental identification of resonant frequencies, the packaged glass-blown shell was mounted on a rotary stage at the focal point of the LDV (Fig. 9). The frequency spectrum of vibrations was measured by driving the piezoelectric substrate with 1 VAC at frequencies ranging from 0.6 to 1.45 MHz and sensing velocity of a single point on the equator. Fig. 10 shows the frequency response of the vibrating shell, revealing mechanical resonances in the megahertz range consistent with theoretical predictions (see Table I).

To experimentally identify mode shapes corresponding to each resonant peak in Fig. 10, the surface velocities of the shell were measured. Due to the axial symmetry of the fabricated sphere, vibratory modes can be uniquely identified by the velocity distribution along the equator. The mode shapes and velocity distribution for one period of vibrations were predicted theoretically for $m = 0, 1, 2, 3$ (see Fig. 4). To measure velocity as a function of the angular position on the shell (longitude), a scan was performed by rotating the packaged device with

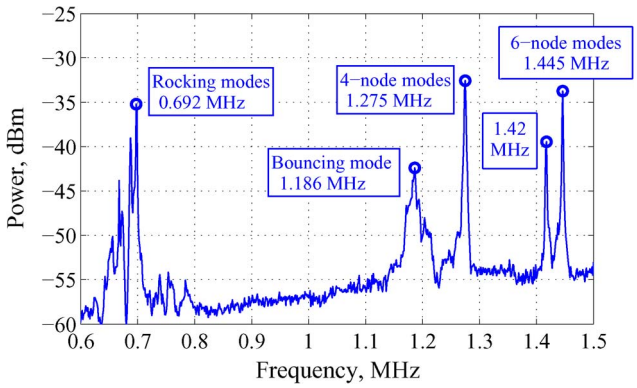

Fig. 10. Frequency response of a 1-mm-scale glass-blown spherical shell, revealing balanced resonant modes in the megahertz range.

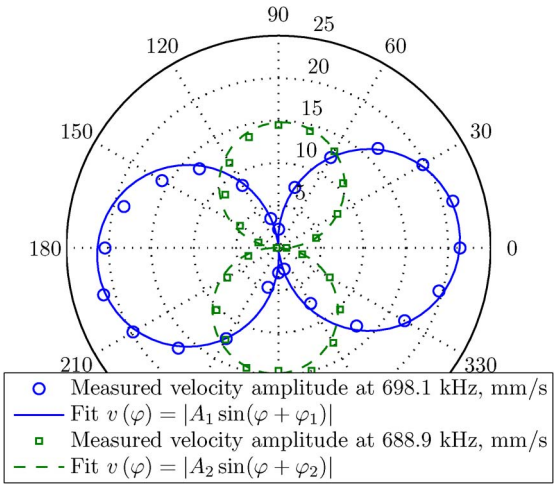

Fig. 11. Measured velocity amplitude distribution along the equator of a spherical shell excited in rocking modes (in polar coordinates).

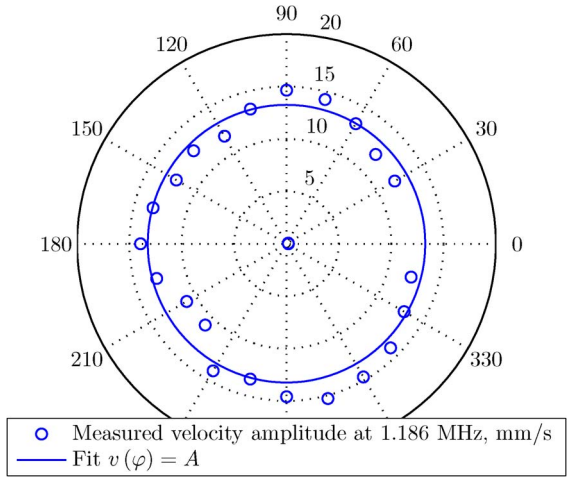

Fig. 12. Measured velocity amplitude distribution along the equator of a spherical shell excited in a bouncing mode (polar coordinates).

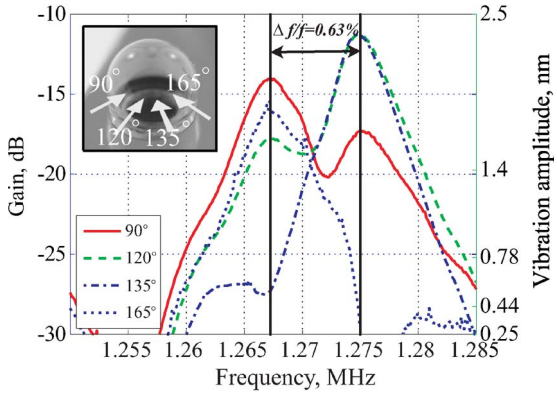

Fig. 13. Measured frequency responses corresponding to the four-node wineglass modes, revealing a relative frequency mismatch $\Delta f/f$ of only 0.63%.

respect to the stationary LDV beam in 15° increments of longitude. The positioning error limited the accuracy of the velocity measurements to within ±1 mm/s.

1) Rocking Modes: The velocity amplitudes of the shell vibrating at 0.689 and 0.698 MHz were measured at 24 equally spaced points along the equator and were plotted in polar coordinates (Fig. 11). The fit to functions $|A_i \sin(\varphi + \varphi_i)|, i = 1, 2$ revealed two nodes for each velocity map, previously observed in simulated rocking modes $(m = 1)$, shown in Fig. 4(b). As expected from FE modeling, the relative spatial orientation $\varphi_1 - \varphi_2$ between the two degenerate modes is close to 90°.

2) Bouncing Mode: The scanning of vibratory mode at 1.186 MHz revealed a uniform velocity distribution (Fig. 12), proving that the shell was excited in a bouncing mode $(m = 0)$.

3) Balanced Four-Node Wineglass Modes: For the next frequency range between 1.255 and 1.285 MHz, FE modeling suggests two degenerate four-node wineglass modes. To identify the frequency mismatch $\Delta f/f$ between these modes, the frequency responses of the glass-blown shell were collected at several locations on the equator, demonstrating mismatch of only 0.63% with 30 ppm accuracy (Fig. 13). The uncertainty of the $\Delta f/f$ measurements was determined by a frequency resolution of 38 Hz for the current experimental setup. The frequency response at 135° longitude revealed a mechanical quality (Q) factor of 318 in air, which can be improved by operating in a vacuum. Further enhancement is possible by minimizing the shell anchoring to the substrate or by using high-Q materials.

Next, mode shapes corresponding to the two resonant frequencies were analyzed and compared to the theoretical four-node wineglass velocity distributions [Fig. 4(c)]. The velocity maps measured at frequencies of 1.266 and 1.274 MHz exhibit four points with zero displacement, which is a characteristic of a balanced four-node wineglass mode (Fig. 14). The relative spatial orientation between the two four-node wineglass velocity patterns is defined by the principal axes of elasticity. The fit to functions $|A_i \sin(2\varphi + \varphi_i)|$ revealed an angle $\varphi_1 - \varphi_2 = 27°$ between the principal axes of elasticity (Fig. 14).

The deviation from an ideal 45° angle suggests cross coupling between the two theoretically degenerate modes, which can be attributed to the thickness variation in the horizontal cross section. This effect can be reduced by using hard mask lithography for patterning and etching circular cavities or by increasing the anodic bond strength. The next resonant peaks at 1.42 MHz in Fig. 10 were identified as asymmetric four-node modes.

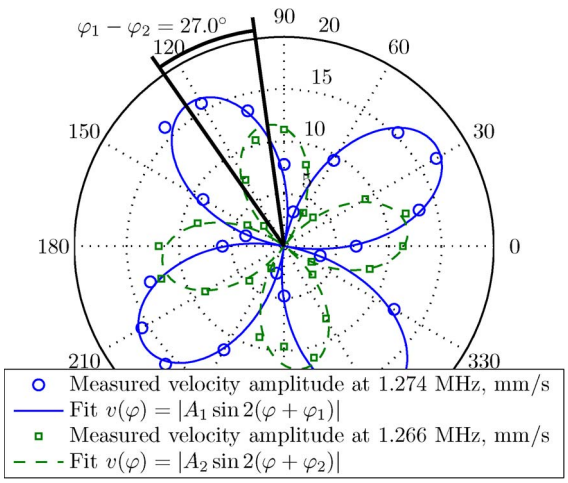

Fig. 14. Measured velocity amplitude distribution along the equator of a spherical shell excited in four-node modes (polar coordinates).

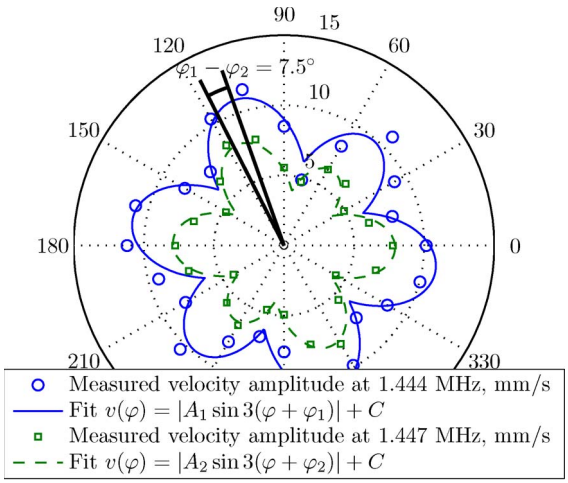

Fig. 15. Measured velocity amplitude distribution along the equator of a spherical shell excited in six-node modes (polar coordinates).

4) Balanced Six-Node Wineglass Modes: The next pair of mechanical resonances was observed at 1.444 and 1.447 MHz, corresponding to the six-node modes of vibrations (Fig. 15). The relative frequency mismatch was 0.2%, with a mechanical Q-factor of 480, demonstrating an improvement over the four-node mode characteristics. Fitting the data to the mode shape $|A_i \sin(3\varphi + \varphi_i)| + C$ revealed a 7.5° angle between the principal axes of elasticity, which deviates from a theoretical value of 30° due to the limitations of soft mask lithography and bonding tools used in the current work.

The mode shapes corresponding to each resonant peak (Fig. 10) were identified experimentally and were summarized in Table I, demonstrating a 7% agreement between the theoretical and measured frequencies for modes $m = 1, 2, 3$. The difference is partially accounted for by a variation in thickness of the vertical cross section of the glass-blown shell [Fig. 2(b)].

Despite the apparent modal cross coupling, the degree of shell symmetry measured in terms of frequency mismatch $\Delta f/f$ remained less than 1%. Moreover, the frequency mismatch shows an improvement for the higher order modes (see Table I). The same phenomenon was observed for high-order composite bulk acoustic resonators [29], confirming that the 3-D resonator operating in mode $m = 3$ is more robust to fabrication imperfections. The tradeoff, however, is the increased number of electrodes required for the selective excitation of high-order modes. The noncontact characterization using off-chip actuation revealed isotropy and principal axis alignment comparable to the state-of-the-art planar silicon MEMS [1], calling for the development of integrated on-chip transducers.

IV. Integration of Transducers

The integration of the electromagnetic and electrostatic transducers with the glass-blown spherical resonators requires definition of conductive traces and electrodes on the curved 3-D surfaces of the spherical structures. Conventional methods such as line-of-sight metal deposition using a shadow mask are not practical due to the aspect ratio limitations.

A. 3-D Metal Fabrication Using Wafer-Scale Glassblowing

Instead of patterning metal conductors on the curved surface of already glass-blown spherical structures, the explored fabrication approach relied on the definition of the metal features prior to the glassblowing step [Fig. 1(a)]. The flat metal features are deposited on top of the Pyrex substrate using, for instance, a lift-off procedure. When the bonded Pyrex–Si wafer stack with patterned metal structures is heated above the 850-°C softening point of glass, spherical glass structures with integrated 3-D metal electrodes and traces are created [Fig. 1(b)].

The main practical challenge of the proposed technique was devising a metal stack that was ductile enough to plastically deform together with the glass substrate during the glassblowing step. At the same time, the metal conductor had to be resistant to degradation during the high-temperature treatment. The initial approach of using a stack of 0.5-μm Au and 0.05-μm Cr was challenging due to the partial segmentation of the continuous traces during the plastic deformation phase of the glassblowing process. This limitation was overcome after multiple design iterations. The successful design was achieved by incorporating an intermediate 0.6-μm-thick layer of ductile Cu between the 0.05-μm Cr adhesion layer and the 0.4-μm Au corrosion-resistant top layer. The relatively thin metal stack, compared to the shell thickness, has a minor effect on the symmetry and surface roughness of glass-blown structures. Figs. 16, 17, and 20 show fabricated samples containing glass-blown spherical shells with integrated 3-D metal electrodes and traces, formed from a flat 200-μm-thick Pyrex glass wafer with patterned Cr-Cu-Au metal stack. These structures were chosen for the initial experimental characterization.

B. Magnetic and Electrostatic Transducers

The successful fabrication of the patterned metal features on the surface of glass-blown spherical structures allowed the integration of electromagnetic and electrostatic transducers. The explored architecture for on-chip electromagnetic transducers utilizes 3-D metal traces on the surface of a glass-blown shell (Fig. 17). The metal trace was patterned as a folded coil to

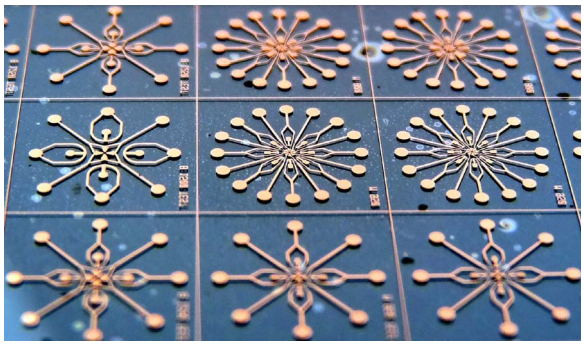

Fig. 16. Photograph of the batch fabricated spherical shell resonators with integrated electrostatic transducers before wafer-level glassblowing.

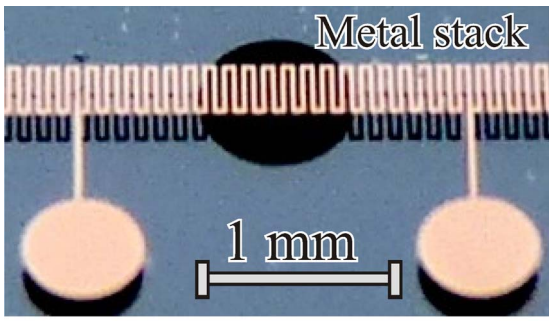

(a)

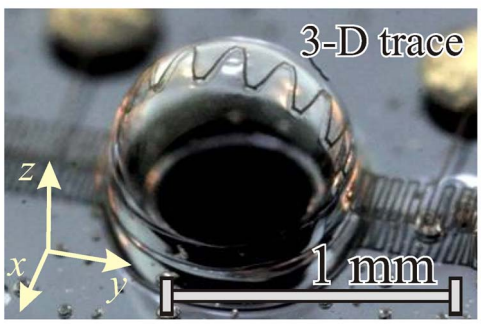

(b)

Fig. 17. Photographs of a continuous metal trace fabricated on a glass-blown spherical shell structure. (a) Metal trace before glassblowing. (b) Metal trace after glassblowing.

account for the stretching of the metal trace during the plastic deformation of the glass shell. The final 3-D geometry of the shell and metal electrodes was defined by the glassblowing step, which created a 20-μm-wide 130-Ω 3-D metal trace across a spherical resonant shell of 1.3 mm in diameter and 20 μm in thickness [Fig. 17(b)].

To generate a magnetic field, a pair of millimeter-scale 0.5-T permanent magnets was bonded to the die on opposite sides of the glass-blown shell (Fig. 18). When current is passed through the metal trace on the spherical shell, a distributed Lorentz force is generated, which is used to excite the mechanical response of the spherical shell. While electromagnetic actuation is commonly used in micro- and nanoscale resonators [30], its drawback is the demanding requirement for strong magnetic fields (on the order of 1 T), which are usually achieved by using external permanent magnets or superconductive coils.

The approach for the definition of metal traces on 3-D structures was also adapted to implement electrostatic transducers

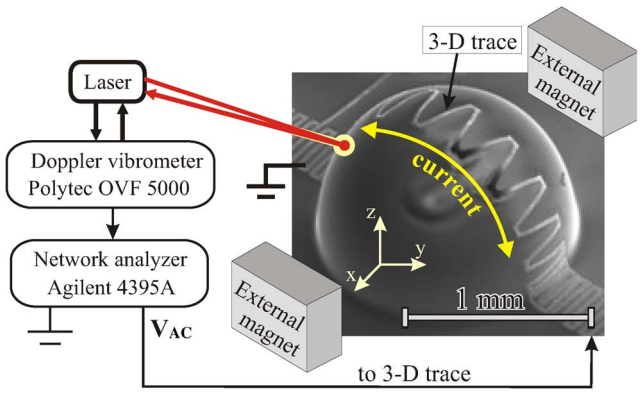

Fig. 18. Schematics of the experimental testbed for on-chip electromagnetic excitation of glass-blown resonant shells.

embedded in glass-blown spherical resonators. The idea behind the design of the 3-D capacitors for electrostatic transduction is to form a large-area high aspect ratio capacitor between the resonant shell and stationary electrodes supported by satellite spherical structures (Figs. 1 and 20). The diameters of the central resonant shell and surrounding satellite shells were approximately 1.3 and 0.85 mm, respectively.

V. Transducer Characterization

The feasibility of the 3-D spherical glass-blown resonators with cofabricated transduction structures was experimentally demonstrated by driving the central resonant shell into mechanical resonance. This section presents the results illustrating on-chip electromagnetic and electrostatic actuation.

A. Electromagnetic Actuation

The operation of the 3-D electromagnetic transducers was characterized experimentally using a spherical shell with integrated 20-μm-wide 130-Ω metal trace running across the shell (Fig. 17). An ac actuation current of 0.2 mA was passed through the metal trace in a magnetic field of 0.5 T generated by the two millimeter-scale permanent magnets (Fig. 18). A Lorentz force on the order of 0.5 μN was generated to initiate vibrations of the glass-blown shell. The mechanical response of the shell was measured using the LDV. Frequency response characterization revealed a 687-kHz resonance, corresponding to a rocking mode of shell vibrations (Fig. 19). While this experiment demonstrated operational 3-D electromagnetic resonators with an integrated actuator, the requirement for relatively high currents and magnetic fields motivated the investigation of alternative transduction approaches.

B. Electrostatic Actuation

The performance of the integrated 3-D electrostatic transducers was characterized using a fabricated prototype with four discrete capacitors formed between the central resonant shell surrounded by the eight smaller satellite structures [Fig. 1(b)]. Unlike the electromagnetic architecture, the electrostatic design ensures a selective excitation of the four-node wineglass mode. Due to its symmetry, the mode provides inherent rejection

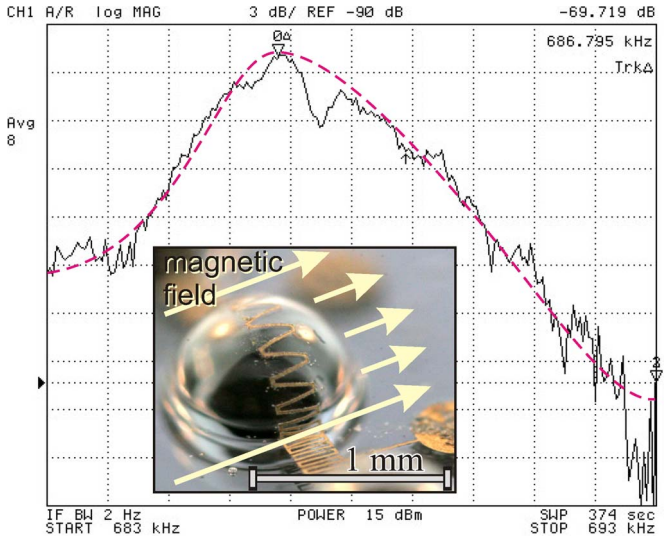

Fig. 19. Measured frequency response of a glass-blown shell actuated in a rocking mode with an on-chip 3-D magnetic transducer, demonstrating feasibility of the actuation approach.

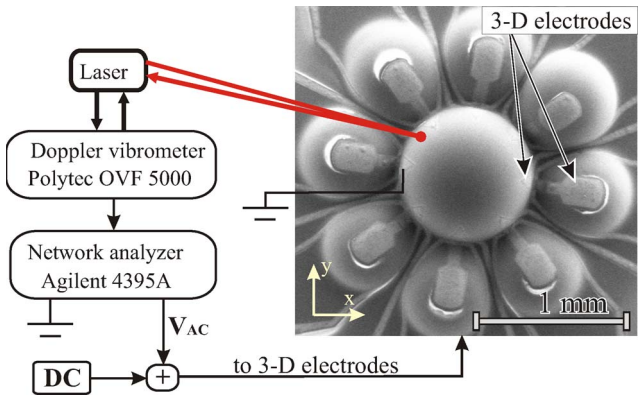

Fig. 20. Schematics of the experimental setup for the on-chip electrostatic excitation of glass-blown resonant shells.

of common mode accelerations and has a potential for high-quality factor and low phase noise operation [1]. To excite vibrations of a central shell, a combination of dc and ac voltages was applied across the capacitors formed between the central and satellite shells (Fig. 20). The mechanical response of the electrostatically excited resonator was characterized by measuring velocities at 36 equally spaced locations along the shell equator using the LDV. A four-node wineglass mode of vibration was identified at 943.7 kHz. Due to the increased diameter of the shell used in the experiment (1.3 mm diameter compared to 1 mm), this resonant frequency differs from previously observed 1.27 MHz. The frequency shift is consistent with the FE modeling.

The velocity amplitude data for the shell equator vibrating at 943.7 kHz were collected and plotted in polar coordinates for further analysis of the mode-shape (Fig. 21). The measurement data show a characteristic pattern of a wineglass mode with four nodes and four points of maximum velocity amplitude. The analysis of the velocity phase data reveals four regions of 180° alternating phase, confirming the four-node wineglass mode.

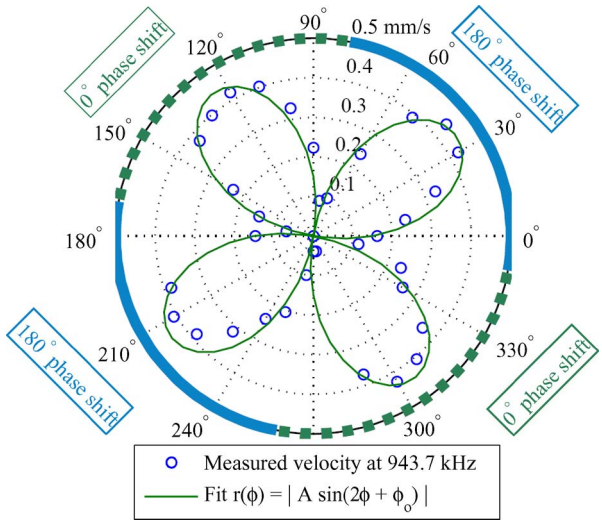

Fig. 21. Measured velocity amplitude and phase distribution along the equator of a spherical shell vibrating in a four-node wineglass mode excited by on-chip capacitive transducers.

These experimental results demonstrate the feasibility of integrated 3-D capacitors for excitation of dynamically balanced wineglass modes in glass-blown spherical shell resonators.

VI. Conclusion

A novel approach for the fabrication of 3-D spherical shell MEMS resonators with cofabricated electromagnetic and electrostatic transduction was presented and experimentally illustrated. The fabrication process takes advantage of plastic deformation driven by gas pressure and surface tension forces (glassblowing) to create smooth, symmetric, and high aspect ratio 3-D structures. The axisymmetric 3-D shell architectures demonstrated surface-roughness-to-height ratio on the order of 1 ppm. The mode shapes and natural frequencies predicted analytically were confirmed experimentally with 7% agreement. Without any trimming or tuning of the natural frequencies, a 1-MHz shell resonator demonstrated a 0.63% frequency mismatch between two degenerate four-node wineglass modes. Excitation at higher order six-node wineglass modes revealed only a 0.2% relative frequency mismatch.

Our preliminary results provide inspiration for further design and fabrication of application-specific architectures of 3-D vibratory MEMS such as resonators and gyroscopes. Even though the presented results are initial steps toward mature dynamic 3-D MEMS, we believe that the approach may lead to high-precision devices with high aspect ratio architectures, efficient low-noise transduction, increased stability, and reduced energy dissipation, thus enabling a new class of inertial instruments and truly exploiting the physics of 3-D elastic waves in symmetric shells on a microscale.

Appendix
Calculation of a Frequency Parameter k_m

Based on general shell-of-revolution equations of equilibrium proposed by Love [17] and later expanded by Novozhilov

[21] in terms of displacement components u, v, and w [Fig. 2(a)], free harmonic vibrations of a thin elastic spherical shell are governed by the partial differential equations [31]

$$\begin{aligned}\Delta U + 2U &= -(1-\nu^2)(F_1+F_2)\\ \Delta V + 2V &= F_3\\ \Delta\Delta w + 2\Delta w + c^2 w &= \frac{c^2}{1-\nu}U + c^2 F_1 + 2(1-\nu^2)F_2 \end{aligned} \quad (3)$$

where Δ is the Laplacian operator, $c^2 = 12(1-\nu^2)R^2/h^2$, and

$$\begin{aligned} U &= \frac{\partial u}{\partial\theta} + u\cot\theta + \frac{1}{\sin\theta}\frac{\partial v}{\partial\varphi} - (1+\nu)w\\ V &= \frac{\partial v}{\partial\theta} + v\cot\theta - \frac{1}{\sin\theta}\frac{\partial u}{\partial\varphi}\\ F_1 &= -\frac{\rho R^2}{E}\frac{\partial^2 w}{\partial t^2}\\ F_2 &= -\frac{\rho R^2}{E}\frac{\partial^2}{\partial t^2}\left[\frac{\partial U}{\partial\theta} + U\cot\theta + \frac{1}{\sin\theta}\frac{\partial V}{\partial\varphi}\right]\\ F_3 &= \frac{2(1+\nu)\rho R^2}{E}\frac{\partial^2}{\partial t^2}\left[\frac{\partial V}{\partial\theta} + V\cot\theta - \frac{1}{\sin\theta}\frac{\partial U}{\partial\varphi}\right]. \end{aligned}$$

U and V are the scalar functions of the displacement components; R and h are the shell radius and thickness, respectively; E and ν are the Young's modulus and Poisson's ratio, respectively; and ρ is the volumetric mass density. The boundary conditions of a spherical shell rigidly clamped at the edge angle $\theta = \alpha$

$$u|_{\theta=\alpha} = v|_{\theta=\alpha} = w|_{\theta=\alpha} = 0 \quad (\partial w/\partial\theta)|_{\theta=\alpha} = 0 \quad (4)$$

together with the partial differential equations (3) define a boundary value problem.

The effect of the boundary conditions on the natural frequencies is studied by applying the method of separation of variables. By substituting functions U, V, and w in the form of Fourier series

$$\begin{aligned} U &= \sum_{m=0}^{\infty} U_m(\theta)\cos(m\varphi)\cos(2\pi f_m t)\\ V &= \sum_{m=0}^{\infty} V_m(\theta)\sin(m\varphi)\cos(2\pi f_m t)\\ w &= \sum_{m=0}^{\infty} w_m(\theta)\cos(m\varphi)\cos(2\pi f_m t) \end{aligned}$$

the system (3) can be reduced to the ordinary differential equations in terms of $w_m = w_m(\theta)$ and $V_m = V_m(\theta)$

$$\begin{aligned} &\Delta\Delta\Delta w_m + (4+k_m^2)\Delta\Delta w_m + c^2\left(1 - \frac{k_m^2}{1-\nu^2}\right)\\ &\times\Delta w_m + c^2\left(2 + \frac{1+3\nu}{1-\nu^2}k_m^2 - \frac{k_m^4}{1-\nu^2}\right)w_m = 0 \quad (5)\\ &\Delta V_m + 2\left(1 + \frac{k_m^2}{1-\nu}\right)V_m = 0 \quad (6) \end{aligned}$$

where k_m is the dimensionless frequency parameter introduced in (1) for the natural frequency of the mth mode and is calculated for each m for a set of boundary conditions. System eqs. (5) and (6) decouple into two independent equations. Equation (6) describes purely tangential motion (u, v) of a spherical shell, while (5) includes also normal vibrations (w). Nevertheless, both equations are taken into account to satisfy the boundary conditions (4).

Each of (5) and (6) is a particular case of the differential equation for spherical harmonics, and their solutions for the spherical shell bounded by one circular boundary are

$$w_m = \sum_{i=1}^{3} A_i P_{n_i}^m(\cos\theta) \quad V_m = A_4 P_{n_4}^m(\cos\theta) \quad (7)$$

where $P_{n_i}^m(\cos\theta)$ is the associated Legendre functions of the first kind of the order m and degree n_i. The set of permissible values n_i is calculated by satisfying the boundary conditions in (4). The degrees n_i are real or complex numbers for the shell with arbitrary boundaries and an integer for the complete spherical shell with no boundary constraints. The values $p_i = n_i(n_i+1)$ are used to solve the characteristic equation of (5)

$$\begin{aligned} k_m^4 - \left[p_i + 1 + 3\nu + (1-\nu^2)\frac{p_i^2}{c^2}\right]k_m^2\\ + (1-\nu^2)\left[p_i - 2 + p_i^2\frac{p_i - 4}{c^2}\right] = 0 \end{aligned} \quad (8)$$

and to determine the frequency parameter k_m. The roots of biquadratic eq. (8) are defined by the coefficients c^2, p_i, and ν, showing that the frequency parameter k_m depends on three physical parameters: thickness-to-radius ratio h/R, edge angle α, and Poisson's ratio ν.

The frequency parameter k_m for each vibratory mode m is calculated by solving characteristic equation (8) and by satisfying the boundary conditions given by (4). The dimensionless values k_m are converted to the spherical shell natural frequencies f_m by using (1).

ACKNOWLEDGMENT

The authors would like to thank the staff of the University of California, Irvine (UCI), Integrated Nanosystems Research Facility and Laboratory for Electron and X-ray Instrumentation for the fabrication and characterization assistance and D. M. Silberman of Physik Instrumente L. P. and Dr. E. J. Eklund of Western Digital Corporation for their insightful discussions. Design, modeling, and characterization were performed using the UCI Microsystems Laboratory research facility.

REFERENCES

[1] C. Nguyen. (2007, Feb.). MEMS technology for timing and frequency control. *IEEE Trans. Ultrason., Ferroelectr., Freq. Control* [Online]. *54(2)*, pp. 251–270. Available: http://ieeexplore.ieee.org/lpdocs/epic03/wrapper.htm?arnumber=4107685

[2] S. Tabatabaei and A. Partridge. (2010, Mar./Apr.). Silicon MEMS oscillators for high-speed digital systems. *IEEE Micro* [Online]. *30(2)*, pp. 80–89. Available: http://ieeexplore.ieee.org/lpdocs/epic03/wrapper.htm?arnumber=5446253

[3] W.-T. Hsu, "Recent progress in silicon {MEMS} oscillators," in *Proc. 40th Annu. PTTI Meeting*, Reston, Virginia, 2008, pp. 135–146.

[4] C. Lam, "A review of the recent development of {MEMS} and crystal oscillators and their impacts on the frequency control products industry," in *Proc. IEEE Ultrason. Symp.*, Nov. 2008, pp. 694–704.
[5] M. J. Madou, *Fundamentals of Microfabrication: The Science of Miniaturization*, 2nd ed. Boca Raton, FL: CRC, 2002.
[6] IEEE Standard Specification Format Guide and Test Procedure for Coriolis Vibratory Gyros, IEEE Std 1431-2004, 2004.
[7] F. Niordson. (1984). Free vibrations of thin elastic spherical shells. *Int. J. Solids Struct.* [Online]. *20(7)*, pp. 667–687. Available: http://linkinghub.elsevier.com/retrieve/pii/0020768384900234
[8] K. D. Wise, M. G. Robinson, and W. J. Hillegas. (1981, Apr.). Solid-state processes to produce hemispherical components for inertial fusion targets. *J. Vac. Sci. Technol.* [Online]. *18(3)*, pp. 1179–1182. Available: http://link.aip.org/link/?JVS/18/1179/1&Agg=doi
[9] H. Hashimoto, S. Tanaka, K. Sato, I. Ishikawa, S. Kato, and N. Chubachi. (1993, May). Chemical isotropic etching of single-crystal silicon for acoustic lens of scanning acoustic microscope. *Jpn. J. Appl. Phys.* [Online]. *32(5B)*, pt. 1, pp. 2543–2546. Available: http://jjap.ipap.jp/link?JJAP/32/2543/
[10] Y. Desta, M. Murphy, J. Goldie, J. Kiley, and R. Howatt, "Fabrication of micromachined resonating cylinder gyroscopes," in *Proc. Book Abstract 4th Int. Workshop HARMST*, Baden-Baden, Germany, 2001, pp. 259–260.
[11] V. S. Ilchenko, M. L. Gorodetsky, X. S. Yao, and L. Maleki. (2001, Mar.). Microtorus: A high-finesse microcavity with whispering-gallery modes. *Opt. Lett.* [Online]. *26(5)*, pp. 256–258. Available: http://www.opticsinfobase.org/abstract.cfm?URI=ol-26-5-256
[12] D. H. Broaddus, M. A. Foster, I. H. Agha, J. T. Robinson, M. Lipson, and A. L. Gaeta. (2009, Apr.). Silicon-waveguide-coupled high-*Q* chalcogenide microspheres. *Opt. Exp.* [Online]. *17(8)*, pp. 5998–6003. Available: http://www.opticsinfobase.org/abstract.cfm?URI=oe-17-8-5998
[13] J. Schroers, Q. Pham, A. Peker, N. Paton, and R. V. Curtis. (2007, Aug.). Blow molding of bulk metallic glass. *Scripta Mater.* [Online]. *57(4)*, pp. 341–344. Available: http://linkinghub.elsevier.com/retrieve/pii/S1359646207003132
[14] S. Zotov, I. Prikhodko, A. Trusov, and A. Shkel, "3-D micromachined spherical shell resonators with integrated electromagnetic and electrostatic transducers," in *Proc. Solid State Sens., Actuator Microsyst. Workshop*, Hilton Head Island, South Carolina, 2010, pp. 11–14.
[15] E. J. Eklund and A. M. Shkel. (2007, Apr.). Glass blowing on a wafer level. *J. Microelectromech. Syst.* [Online]. *16(2)*, pp. 232–239. Available: http://ieeexplore.ieee.org/lpdocs/epic03/wrapper.htm?arnumber=4147583
[16] E. J. Eklund, A. M. Shkel, S. Knappe, E. Donley, and J. Kitching. (2008, May). Glass-blown spherical microcells for chip-scale atomic devices. *Sens. Actuators A, Phys.* [Online]. *143(1)*, pp. 175–180. Available: http://linkinghub.elsevier.com/retrieve/pii/S0924424707007145
[17] A. Love, *A Treatise on the Mathematical Theory of Elasticity*. Cambridge, U.K.: Cambridge Univ. Press, 1927.
[18] A. van der Neut, *De Elastische Stabiliteit van den Dunwandigen Bol*. Amsterdam, The Netherlands: H.J. Paris, 1932.
[19] A. Havers, "Asymptotische biegetheorie der unbelasteten kugelschale," *Arch. Appl. Mech.*, vol. 6, no. 4, pp. 282–312, Aug. 1935.
[20] K. Federhofer, "Eigenschwingungen der kegelschale," *Arch. Appl. Mech.*, vol. 9, no. 4, pp. 288–308, Aug. 1938.
[21] V. Novozhilov, "Stress analysis in a thin spherical shell under arbitrary load," *Proc. USSR Acad. Sci. (Dokl. Akad. Nauk SSSR)*, vol. 27, no. 6, pp. 537–540, 1940.
[22] V. Novozhilov, *The Theory of Thin Shells*. Groningen, The Netherlands: Noordhoff, 1959.
[23] R. Blevins, *Formulas for Natural Frequency and Mode Shape*. New York: Van Nostrand, 1979.
[24] E. J. Loper, D. D. Lynch, and K. M. Stevenson, "Projected performance of smaller hemispherical resonator gyros," in *Proc. IEEE PLANS*, Las Vegas, NV, 1986, pp. 61–64.
[25] C. T.-C. Nguyen, "Micromechanical signal processors," Ph.D. dissertation, Univ. California, Berkeley, CA, 1994.
[26] P.-G. de Gennes, F. Brochard-Wyart, and D. Quere, *Capillarity and Wetting Phenomena: Drops, Bubbles, Pearls, Waves*. Berlin, Germany: Springer-Verlag, 2004.
[27] V. I. Goleus, A. Y. Belyi, M. Sardak, and Y. I. Belyi. (1996, Aug.). Calculation of the surface tension of molten borosilicate glasses. *Glass Ceram.* [Online]. *53(8)*, pp. 226–228. Available: http://www.springerlink.com/index/10.1007/BF01213775
[28] V. Braginsky, V. Mitrofanov, and V. Panov, *Systems With Small Dissipation*. Chicago, IL: Univ. Chicago Press, 1985.
[29] G. K. Ho, R. Abdolvand, and F. Ayazi, "High-order composite bulk acoustic resonators," in *Proc. Int. Conf. Micro Electro Mech. Syst.*, Jan. 2007, pp. 791–794.
[30] A. N. Cleland and M. L. Roukes, "Fabrication of high frequency nanometer scale mechanical resonators from bulk Si crystals," *Appl. Phys. Lett.*, vol. 69, no. 18, pp. 2653–2655, Oct. 1996.
[31] I. P. Prikhodko, S. A. Zotov, A. A. Trusov, and A. M. Shkel, "Mechanical characterization of micromachined glass-blown 3-D spherical shells," in *Proc. Nanotech*, vol. 2, Anaheim, CA, Jun. 20–24, 2010, pp. 300–303. [Online]. Available: http://www.nsti.org/procs/Nanotech2010v2/6/W22.903

Igor P. Prikhodko (S'09) received the B.S. and M.S. degrees (*cum laude*) in applied mathematics and mechanics from Moscow State University, Moscow, Russia, in 2007, and the M.S. degree in mechanical and aerospace engineering from the University of California, Irvine, in 2008, where he is currently working toward the Ph.D. degree in the MicroSystems Laboratory.

He serves as a reviewer for major MEMS journals. His research focus is the full cycle development of MEMS inertial sensors and 3-D shell resonators.

Mr. Prikhodko is a member of the American Society of Mechanical Engineers.

Sergei A. Zotov (M'11) received the M.S. and Ph.D. degrees in mechanical engineering and control systems from Tula State University, Tula, Russia, in 1999 and 2002, respectively.

He is currently a Postdoctoral Scientist in the MicroSystems Laboratory, University of California, Irvine, where he is responsible for the design, fabrication, and testing of micromachined devices and systems for inertial navigation. Over the last ten years, his focus has been on MEMS accelerometers and gyroscopes. He is the holder of eight Russian patents, with three U.S. patents pending.

Alexander A. Trusov (S'06–M'09) received the B.S. and M.S. degrees in applied mathematics and mechanics from Moscow State University, Moscow, Russia, in 2004, and the M.S. and Ph.D. degrees in mechanical and aerospace engineering from the University of California, Irvine (UCI), in 2006 and 2009, respectively.

He is currently a Project Scientist in the MicroSystems Laboratory, UCI, where he leads several programs on high-performance inertial microsystems. He has published nine journal and 21 conference papers on MEMS and signal processing, has seven pending U.S. patents on inertial MEMS design, fabrication, and control, and serves as a reviewer for major journals in the fields of MEMS and sensors. His research interests include design, modeling, fabrication, and vacuum packaging of micromachined inertial systems; design of characterization experiments; and statistical data processing and analysis.

Dr. Trusov is a member of the American Society of Mechanical Engineers.

Andrei M. Shkel (S'95–A'98–SM'08) received the Diploma degree (with excellence) in mechanics and mathematics from Moscow State University, Moscow, Russia, in 1991, and the Ph.D. degree in mechanical engineering from the University of Wisconsin, Madison, in 1997.

He is a Program Manager in the Microsystems Technology Office, Defense Advanced Research Projects Agency, Arlington, VA. He is serving in this capacity while on leave from his faculty position as a Professor in the Department of Mechanical and Aerospace Engineering, University of California, Irvine (UCI), where he is also the Director of the UCI Microsystems Laboratory. He is the holder of 15 U.S. and international patents. His professional interests are reflected in more than 120 publications.

Dr. Shkel is an Editor of the JOURNAL OF MICROELECTROMECHANICAL SYSTEMS. He was the recipient of the 2002 George E. Brown, Jr., Award, a 2005 NSF CAREER Award, the 2006 UCI Research Award, and the 2009 Research Award from the IEEE Sensors Council.